sciendo

ANNALS OF WEST UNIVERSITY OF
TIMISOARA PHYSICS

Vol. LXVII, 2025

DOI: 10.2478/awutp-2025-0001

STUDY OF THE PREPLASMA GENERATION FOR FLAT AND NANOSTRUCTURED TARGETS IN CASE OF OBLIQUE RADIATION INCIDENCE

A. Zubarev,[1, 3,*] J. F. Ong[1], A. C. Berceanu[1], M. Cuzminschi[2], and O. Tesileanu[1]

[1]*Extreme Light Infrastructure, Horia Hulubei National Institute of Physics and Nuclear Engineering, IFIN-HH, 30 Reactorului Street, Magurele, RO-077125, Romania*
[2]*Department of Theoretical Physics, Horia Hulubei National Institute of Physics and Nuclear Engineering, IFIN-HH, 30 Reactorului Street, Magurele, RO-077125, Romania*
[3]*National Institute for Plasma Laser and Radiation Physics, Atomistilor street, Magurele, RO-077125, Romania;*
**alxzubarev@gmail.com*

Article Info

Received: 06.12.2024
Accepted: 27.01.2025

Keywords:
prepulse, preplasma, reflection

Abstract

In this proceeding, we compare the preplasma generation in front of the flat and nanostructured targets for different angles of laser incidence. We use radiation-hydrodynamic FLASH code to simulate the laser prepulse interaction with aluminum foil and aluminum nanowire array with aluminum support. During the preplasma evolution, we observe the following stages: heating of the target, generation of preplasma cloud, nanowire implosion and the increase of preplasma density in front of the target, generation of the overcritical-density regions in front of the regions, and joining of the overcritical density regions into a continuous overcritical density layer. The rate of preplasma generation varies in function of the tilting angle. For small tilting angles it decreases with its variation. The rate of preplasma generation is minimal for the tilting angle of about 15 degrees. For lower and higher values of the tilting angle, the preplasma generation ratio is greater. Back-reflection for the nanostructured targets is lower than for the flat target. Its value also depends on the angle of laser incidence. This aspect can potentially increase the safety and the performance of the experiments.

1. Introduction

High-intensity lasers pave the way for promising applications, such as compact particle accelerators [1], high-brilliance γ-ray sources [2], and environment preparation for observation of astrophysical phenomena [3]. To ensure the generation of high-quality monoenergetic particle beams two factors are important: radiation penetration in the depth of the target and high laser intensity. Both the intensity dependence on time of the laser beam and target structure are crucial for laser-driven experiments [4, 5]. Optimizing the quality of laser beams allows us to obtain monoenergetic particle beams for medical applications, surface treatments, and tomography [6, 7].

The quality of the laser pulse is determined by the beam spectra and temporal evolution of the laser intensity. Due to the technical limitations of the chirped pulse amplification technique [8], an ideal laser prepulse with an instantaneous increase of the radiation intensity is challenging. In this way, the laser pulse consists of the ns-ASE pedestal with constant intensity, ps-ramp with exponentially increasing power, and an ultra-short high-intensity main pulse [9, 10].

The usual ns-ASE piedestal duration is from 250 ps to 5 ns and its power is 10^{11} – 10^{12} for PW-class lasers. At this stage the target surface is above the melting point and evaporation starts. The prepulse power is almost constant, but some small fluctuations and secondary peaks have place. At the ps-ramp stage, the laser power increases almost exponentially. The ps-ramp duration is usually 20 – 50 ps. At this stage, laser power increases up to 10^3 times.

The laser prepulse has low intensity, but due to the long duration, it transfers a significant amount of energy into the target. The prepulse interaction leads to the target heating, vaporization, and preplasma generation [11]. Further target irradiation, in case of long prepulse, leads to an increase in the preplasma density due to radiation pressure [12].

Modern high-intensity lasers have contrasts up to 10^{-12}, which means the prepulse intensity is 10^{12} times lower than the intensity of the main pulse [13]. Some specific techniques are used for additional reduction of the prepulse intensity [14], however, the laser prepulse impact remains considerable for multi-Petawatt lasers [15, 16, 17].

The effects of prepulse target interaction depend on the target structure. Modern laser-driven experiments use nanostructured targets with decorative elements such as nanowire arrays, nanocones, or microspheres. The nanostructured surface of the target ensures deeper laser radiation penetration and more uniform heating of the target [18]. During the prepulse, the surface decorations absorb more heat compared to the base of the target. If the laser contrast is low and prepulse power is high, the nanostructures can be destroyed. This fact should be analyzed carefully because deconstruction of the decorative elements can decrease performance of laser-driven experiments. The evaporated substance is ionized fast and in this way the preplasma is generated. During the prepulse, the preplasma quantity incereses and its density changes.

The study of laser prepulse interaction with a nanowire array in the case of normal incidence is presented in the article [10]. The authors reproduce and investigate the real profile of the ELI-NP laser, and conclude that the nanowires implosion and generation of the overcritical density regions cannot be prevented in this experimental configuration. In this way, the performance of the laser-driven experiments decreases [19, 20].

We investigate the relation of laser incidence angle to the preplasma generation, nanowires implosion, and back-reflection. We study the temporal evolution of electron density distribution and back-reflection for reproduced laser prepulse. The results of the numerical simulations and identified recommendations for the experimental setups are presented below.

2. Simulation Details

We used radiation-hydrodynamic FLASH code to implement numerical simulations of prepulse target simulations. We chose standard hydrodynamic solvers completed with multi-temperature treatment. The plasma components and radiation in the simulation domain are out of the thermal equilibrium. The heat exchange contributes to the energy transfer between the electron and ions. The simulation program tracks the energy deposition via the inverse Bremsstrahlung effect. Material properties such as the equation of state (EOS), average ionization state, and opacities are obtained from ionmix4 tabulated data. Radiation diffusion is incorporated using the multi-group diffusion (MGD) theory [21]. The MGD simulations are effectuated using 6 groups from 10^{-1} to 10^{5}. The boundary conditions are the following: vacuum for radiation diffusion and zero temperature gradient at the simulation boundaries. The thermal exchange is described using the Spitzer model for heat transfer and flux coefficient not over 0.06 for electron conductivity.

The simulation dimensions have the size 30 micrometers along the x-axis and 20 micrometers along the y-axis. We consider two cases: the flat target and the nanostructured target. For the flat target case, we consider an aluminum plate with a flat surface. For the nanostructured one, we examined an aluminum nanowire array deposited on an aluminum substrate. The nanowire's length is 5 micrometers. We take the diameter of the nanowire of 300 nm and the distance between the nanowires of 1.0 μm. The aluminum density is 2.7 g/cm^{-3}.

We assume the laser wavelength of 800 nm. The beam has Gaussian spatial distribution with the form $I(r_x) = I_0 \exp(r^2_x / R^2_x)$, where $R_x = 2$ μm. The temporal profile of the laser intensity is reproduced from experimental results obtained at 1 PW ELI-NP laser. It is presented in the Figure 1. During the laser prepulse, the laser intensity does not exceed 10^{14} W/cm^2. It allows us to neglect the ionization effects farther than Al^{2+} and apply the radiation-hydrodynamic simulations until the end of the prepulse [22, 23]. The laser contrast (the main pulse over prepulse intensity) is about 10^{11} during the amplified spontaneous emission pedistal (ASE-pedestal).

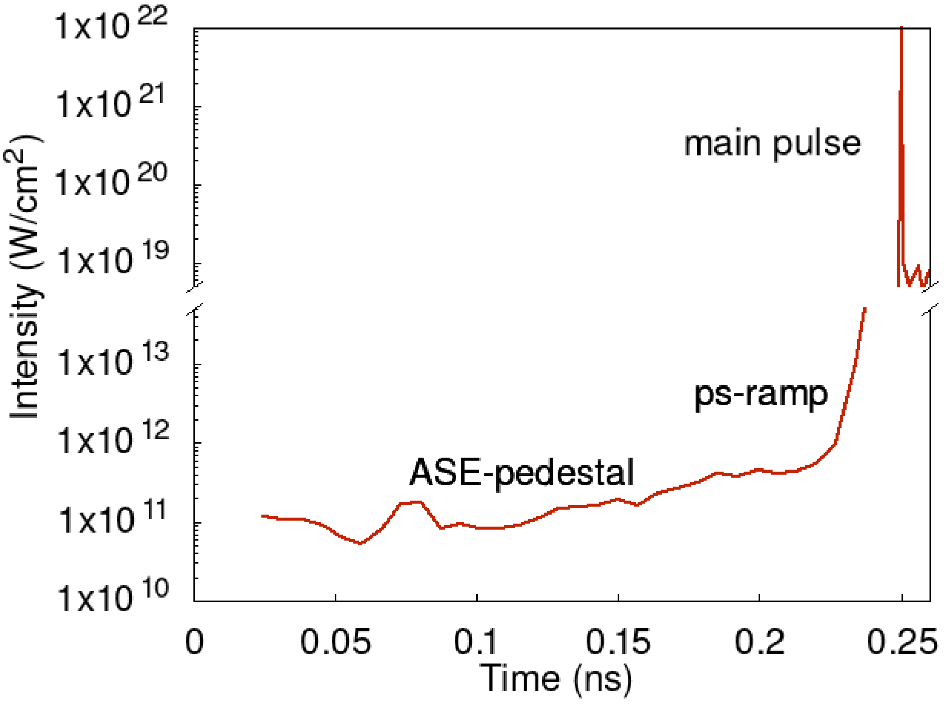

Figure 1. The laser intensity dependence on time. The ASE-pedestal, ps-ramp, and main pulse are put in evidence

To make the simulations closer to reality, we hold the boundaries of the solid target for temperatures below the evaporation point. In this way, we define during the simulation the stage of the solid target with fixed target and the preplasma expansion stage.

3. Preplasma generation and implosion

During the work, we have implemented several simulations for prepulse target interaction for flat and nanostructured targets for different angles of incidence. Preplasma generation is observed for all target geometries and angles of radiation incidence. Due to more intense laser radiation absorption, the amount of the preplasma generated in front of the nanostructured targets is higher than in the case of solid targets.

The preplasma critical density is calculated using the formula:

$$n_{cr} = \frac{\varepsilon_0 m_e}{e^2} \frac{4\pi^2 c^2}{\lambda^2} \tag{1}$$

where ε_0 is vacuum dielectric permittivity, m_e is electron mass, e is charge of electron, c is speed of light, and λ is laser wavelength. The critical density is the maximal density for which the prepulse radiation can penetrate the preplasma cloud and heat the target. For higher than critical densities, the laser radiation is attenuated in the preplasma. For the assumed laser parameters, the critical density is 1.74×10^{21} cm^{-3}.

First, we compared the electron density distribution generated in front of flat and nanostructured targets (Fig. 2). The preplasma generated in front of the nanostructured target is less dense than in front of the flat targets. However, the overcritical density regions are present in both cases. The prepulse radiation intensity is high enough to increase the density of preplasma in front of the nanowires, but the form of the nanowires is preserved (Fig. 2 (b)). This stage marks the start of nanowires implosion.

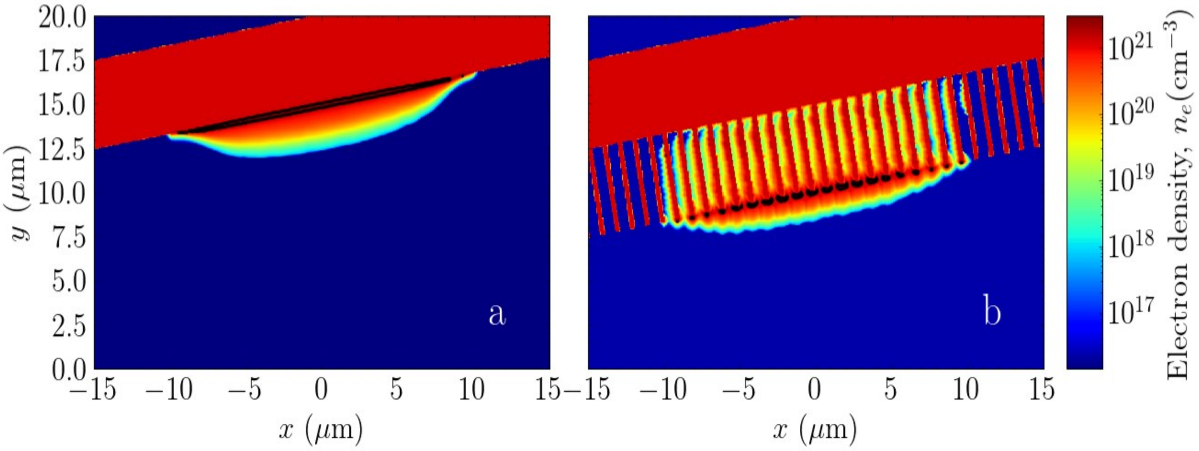

Figure 2. Preplasma generated in front of the (a) solid and (b) nanostructured target upon the influence of laser prepulse for 1 PW laser for target tilted at 5 degrees at normal direction. The time is 25 ps before the main pulse. The solid black lines correspond to the margins of the overcritical density region. The laser radiation propagates along the *y*-axis direction

In Fig. 3 we show preplasma evolution for the target tilted 5 degrees from normal incidence. The temporal evolution of preplasma shows at first (a) generation of preplasma islands around the nanowires in the focus of laser prepulse. During the next stage (b), the preplasma volume increases and a continuous preplasma layer is generated. At 30 ps before the main pulse (c), we observe the generation of the first overcritical density regions in front of the nanowires due to implosion. Finally, the growth of overcritical density islands leads to the generation of a continuous overcritical plasma layer (Fig. 3 (d)).

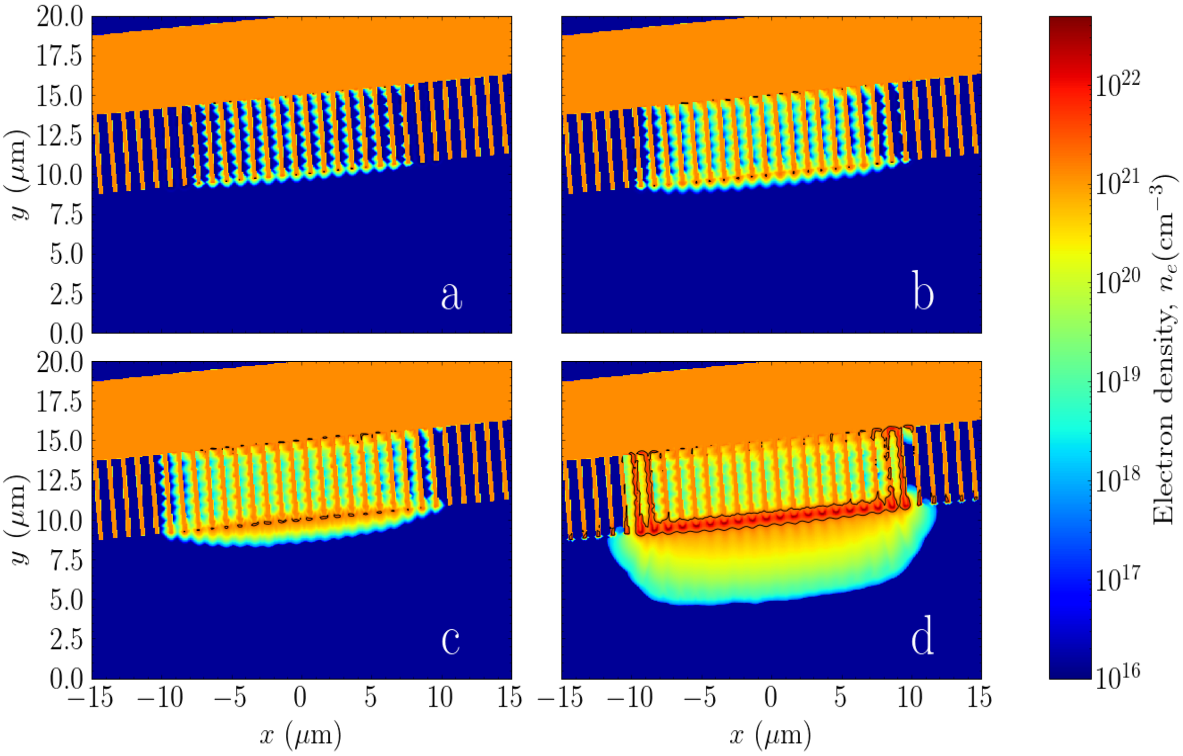

Figure 3. Temporal evolution of preplasma density distribution upon the laser prepulse (a) −114 ps (the preplasma appears), (b) −60 ps, (c) −30 ps (overcritical density regions appears), (d) −2 ps (the end of the hydrodynamic simulation), the target is tilted 5 degrees from the normal direction. The solid black lines correspond to the margins of the overcritical density regions. The laser radiation propagates along the y-axis direction

The preplasma distribution close to the end of prepulse (−15 ps) for different angles is presented in Figure 4. In this figure, we put in evidence the shapes of the preplasma cloud and the size of the overcritical density regions. We study the influence of tilting angle on the preplasma generation and expansion. We observe that for tilting angles from 5 to 15 degrees, the overcritical density regions are joined into a continuous overcritical density layer. In Figure 4 (d) we present the case of 30 degrees. In this instance, the preplasma cloud is the largest, but the overcritical density regions don’t form a continuous layer. This fact can make high tilting angles favorable for some experiments.

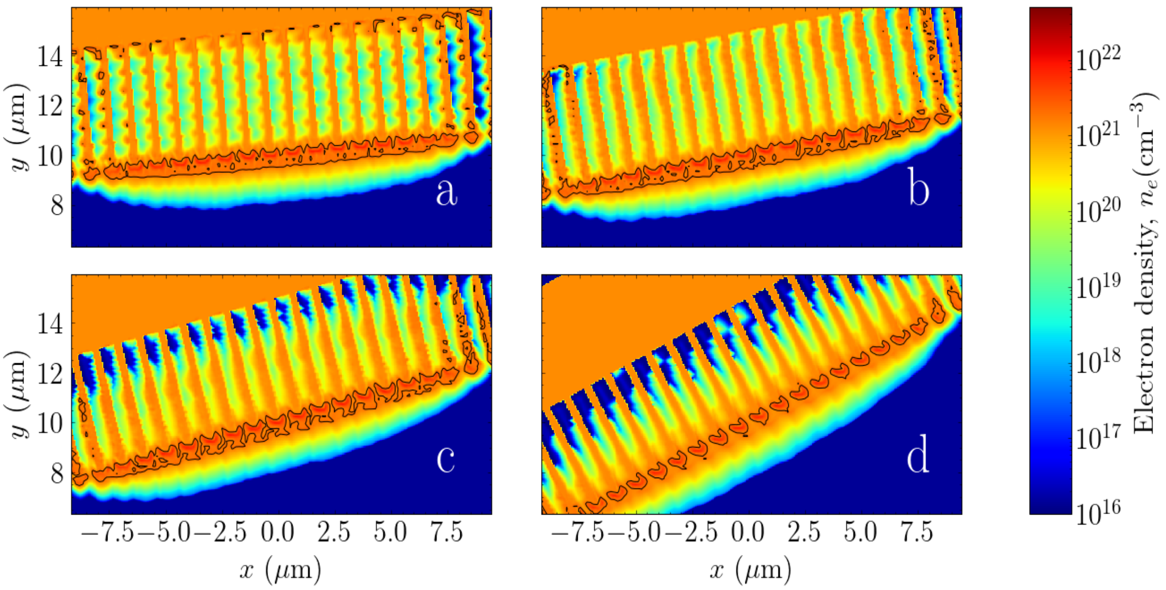

Figure 4. Temporal evolution of preplasma density distribution upon the laser prepulse tilted (a) 5 degrees from the normal incidence, (b) 10 degrees from the normal incidence, (c) 15 degrees from normal incidence, and (d) 30 degrees from the normal incidence for the time −15 ps close to the end of the hydrodynamic simulation. The solid black lines correspond to the margins of the overcritical density region. The laser radiation propagates along the y-axis direction.

4. Back-reflection study

As well, we study the ratio between the output and input laser energy for flat and nanostructured targets (Fig. 5). Both targets are tilted to 10 degrees.

The amount of the input energy is equal to the energy received from the laser. The output energy represents the energy of reflected radiation. The back-reflection plays an important role in the safety of the experiment and indicates the performance of the target. The target is heated better if less energy is reflected. The back-reflection coefficient is presented in the figures below.

We also studied integral reflectivity defined as energy reflected from the target till the selected moment t over the energy received from the laser during the prepulse-target interaction. The integral reflectivity is calculated:

$$\Gamma(t) = \frac{\int_0^t P_{out} d\tau}{\int_0^t P_{laser} d\tau} \qquad (2)$$

The ratio between the output radiation power to the prepulse power is presented for the cases of flat and nanostructured targets (Fig. 5 Left). We observe that in both cases the preplasma is generated for almost the same moment, which corresponds to the increase of output power in the plot. With the preplasma expansion, the ratio of output to input power decreases. For the vast majority of the moments, the back-reflection coefficient is lower for a nanostructured target compared to a flat one. For the moment around 10 ps, before the main pulse (0.24 ns in the plot), we observe the generation of the overcritical density layer, characterized by a fast increase of the reflected power. At this stage, there is no significant difference between the flat and the nanostructured targets. However, due to the relativist icinduced transparency, the main pulse will penetrate the overcritical density layer unless the density is not too high. In this way, the nanostructured target will reflect less radiation than a flat one.

In figure 5 (Right) we present the evolution of integral reflectivity during the prepulse target interaction for flat and nanostructured (array) targets for a tilting angle of 10 degrees. During the interaction, the targets have a little different behavior. Flat targets have higher reflectivity until the generation of the overcritical density layer. For higher times the integral reflectivity is almost the same for the flat and nanostructured targets.

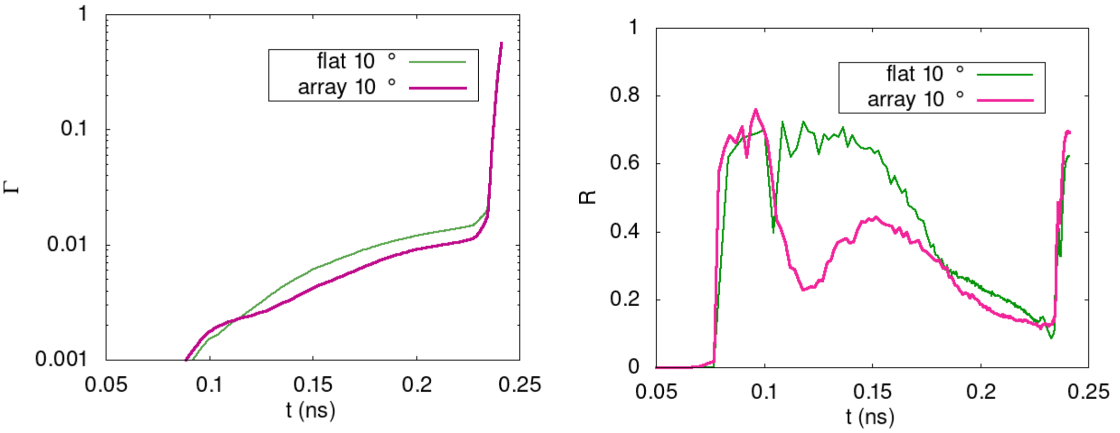

Figure 5. Temporal evolution output over input energy rate (Left) and integral reflectivity (Right) for the flat (green) and nanostructured (magenta) targets. The tilting angle is equal to 10 degrees.

In Figure 6 (Left) we compared the ratio of output to input power for different tilting angles for a nanostructured target. We observe that the power ratio profiles have the same dependence on time. The best result is achieved for the tilting angle of 15 degrees. For tilting angles of 5 and 30 degrees, the ratio of outcome to income powers is higher than for the tilting angle of 15 degrees for the time over 0.2 ns. The overcritical density regions occur almost at the same time for all targets.

In figure 6 (Right) we compared the integral reflectivity for different angles of laser incidence. The value of integral reflectivity increases almost in the same mode for different angles. Generation of the overcritical density plasma in front of the target leads to fast increase of the integral reflectivity.

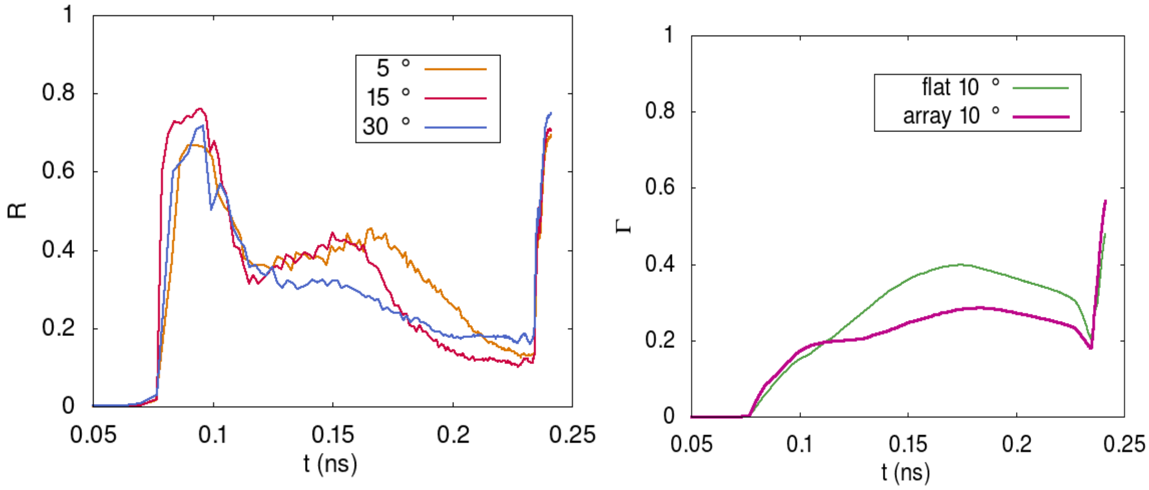

Figure 6. Temporal evolution output over input energy rate (Left) and integral reflectivity for a nanostructured target. The tilting angles are 5 (orange), 15 (red), and 30 (blue) degrees.

5. Conclusions

Two aspects of the prepulse interaction with a solid target were studied: the target structure and the radiation angle of incidence. During the research, we observed that the surface of the flat target is heated faster than the surface of the nanostructured target, and the radiation does not reach the full depth of the structure in the flat target case. The preplasma cloud grows fast, and a thick continuous overcritical density layer is generated in front of the flat target. In the case of the nanostructured target, a part of the laser prepulse radiation is absorbed in the ends of the nanowires.

The preplasma ablated in the nanowire regions gives the onset for the overcritical density islands. Moderate tilting of the target reduces the rate of the preplasma generation and back-reflection. We estimate the optimal angle of the target tilting to be around 15 degrees.

The preplasma generation and expansion strongly influence the rate of reflected radiation. First, the rate of reflected radiation decreases with the target heating, but after the generation of the overcritical density layer increases drastically. The rate of reflected radiation is always greater for a flat target in comparison with a nanostructured one.

The implemented research helps to plan laser-driven experiments with nanostructured targets in order to obtain the optimal target heating and particle acceleration. The study is also important for laser surface treatment.

Acknowledgments

This work was supported by Extreme Light Infrastructure Nuclear Physics (ELI-NP) Phase II, a project co-financed by the Romanian Government and the European Union through the European Regional Development Fund — the Competitiveness Operational Programme (1/07.07.2016, COP, ID 1334) and by the Project PN 23210105, Phase 1, funded by the Ministry of Research, Innovation and Digitalization. The ELI-RO project is supported by the Romanian Government through the Grant Programme ELI-RO-07. We acknowledge the Laser System Department at ELI-NP for providing the data of laser contrast. The software used in this work was developed in part by the DOE NNSA and DOE Office of Science-supported Flash Center for Computational Science at the University of Chicago and the University of Rochester.

References

[1] X.-L. Zhu, M. Chen, S.-M. Weng, T.-P. Yu, W.-M. Wang, F. He, Z.-M. Sheng, P. McKenna, D. A. Jaroszynski, and J. Zhang, *Extremely brilliant gev γ-rays from a two-stage laser-plasma accelerator,* Science advances 6, eaaz7240 (2020).

[2] A. Macchi, M. Borghesi, and M. Passoni, I*on acceleration by superintense laser-plasma interaction*, Reviews of Modern Physics 85, 751–793 (2013).

[3] H. Takabe and Y. Kuramitsu, *Recent progress of laboratory astrophysics with intense lasers*, High Power Laser Science and Engineering 9, e49 (2021).

[4] M. Kirchen, S. Jalas, P. Messner, P. Winkler, T. Eichner, L. Hübner, T. Hülsenbusch, L. Jeppe, T. Parikh, M. Schnepp, A. R. Maier, O*ptimal beam loading in a laser-plasma accelerator*, Physical review letters 126, 174801 (2021).

[5] L. Rovige, J. Huijts, I. Andriyash, A. Vernier, M. Ouillé, Z. Cheng, T. Asai, Y. Fukuda, V. Tomkus, V. Girdauskas, R. Lopez-Martens, J. Faure, *Optimization and stabilization of a kilohertz laser-plasma accelerator*, Physics of Plasmas 28 (2021).

[6] L. Labate, D. Palla, D. Panetta, F. Avella, F. Baffigi, F. Brandi, F. Di Martino, L. Fulgentini, A. Giulietti, P. Köster, D. Terzani, P. Tomassini, C. Traino, L. A. Gizz, *Toward an effective use of laser-driven very high energy electrons for radiotherapy: Feasibility assessment of multi-field and intensity modulation irradiation schemes*, Scientific reports 10, 17307 (2020).

[7] B. Mao, A. Siddaiah, Y. Liao, and P. L. Menezes, *Laser surface texturing and related techniques for enhancing tribological performance of engineering materials: A review*, Journal of Manufacturing Processes 53, 153–173 (2020).

[8] M. R. Edwards and P. Michel, *Plasma transmission gratings for compression of high-intensity laser pulses*, Physical Review Applied 18, 024026 (2022).

[9] J. M. Mikhailova, A. Buck, A. Borot, K. Schmid, C. Sears, G. D. Tsakiris, F. Krausz, and L. Veisz, *Ultra-high-contrast few-cycle pulses for multipetawatt-class laser technology*, Optics letters 36, 3145–3147 (2011).

[10] J. Ong, A. Zubarev, A. Berceanu, M. Cuzminschi, and O. Tesileanu, *Nanowire implosion under laser amplified spontaneous emission pedestal irradiation*, Scientific Reports 13, 20699 (2023).

[11] C. Iorga, *Dynamical aspects of photoionization from the 1s22snp 1Po1 levels belonging to the c iii ion near the first ionization threshold*, Phys. Rev. A 107, 033115 (2023).

[12] R. Nuter, L. Gremillet, P. Combis, M. Drouin, E. Lefebvre, A. Flacco, and V. Malka, *Influence of a preplasma on electron heating and proton acceleration in ultraintense laser-foil interaction*, Journal of applied physics 104 (2008).

[13] E. G. Gamaly, A. V. Rode, B. Luther-Davies, and V. T. Tikhonchuk, *Ablation of solids by femtosecond lasers: Ablation mechanism and ablation thresholds for metals and dielectrics*, Physics of plasmas 9, 949–957 (2002).

[14] J. Nikl, M. Jirka, M. Matys, M. Kucharík, and O. Klimo, *Contrast enhancement of ultra-intense laser pulses by relativistic plasma shutter*, in High Power Lasers and Applications, Vol. 11777 (SPIE, 2021) pp. 107–112.

[15] T. J. Yu, S. K. Lee, J. H. Sung, J. W. Yoon, T. M. Jeong, and J. Lee, *Generation of high-contrast, 30 fs, 1.5 pw laser pulses from chirped-pulse amplification ti: sapphire laser*, Optics express 20, 10807–10815 (2012).

[16] N. Minkovski, S. M. Saltiel, G. I. Petrov, O. Albert, and J. Etchepare, *Polarization rotation induced by cascaded third-order processes*, Opt. Lett. 27, 2025–2027 (2002).

[17] G. Doumy, F. Quéré, O. Gobert, M. Perdrix, P. Martin, P. Audebert, J. C. Gauthier, J.-P. Geindre, and T. Wittmann, *Complete characterization of a plasma mirror for the production of high-contrast ultraintense laser pulses*, Phys. Rev. E 69, 026402 (2004).

[18] J. Park, R. Tommasini, R. Shepherd, R. A. London, C. Bargsten, R. Hollinger, M. G. Capeluto, V. N. Shlyaptsev, M. P. Hill, V. Kaymak, C. Baumann, A. Pukhov, D. Cloyne, R. Costa, J. Hunter, S. Maricle, J. Moody, and J. J. Rocca, *Absolute laser energy absorption measurement of relativistic 0.7 ps laser pulses in nanowire arrays*, Physics of Plasmas 28, 023302 (2021)

[19] T. Hosokai, K. Kinoshita, A. Zhidkov, K. Nakamura, T. Watanabe, T. Ueda, H. Kotaki, M. Kando, K. Nakajima, and M. Uesaka, *Effect of a laser prepulse on a narrow-cone*

ejection of mev electrons from a gas jet irradiated by an ultrashort laser pulse, Physical review E 67, 036407 (2003).

[20] D. A. Serebryakov and E. N. Nerush, *Effect of a prepulse on the efficiency of gamma-ray generation by a relativistic laser pulse obliquely incident on a planar target,* Quantum Electronics 47, 206 (2017).

[21] B. Fryxell, K. Olson, P. Ricker, F. X. Timmes, M. Zingale, D. Lamb, P. MacNeice, R. Rosner, J. Truran, and H. Tufo, *Flash: An adaptive mesh hydrodynamics code for modeling astrophysical thermonuclear flashes,* The Astrophysical Journal Supplement Series 131, 273 (2000).

[22] C. Iorga and V. Stancalie, *A quantitative study of the forbidden and intercombination transitions arising from the li-like al autoionizing levels*, Canadian Journal of Physics 93, 1413–1419 (2015).

[23] C. Iorga, V. ALIE, and V. Pais, *A study of the laser-produced aluminum plasma by means of computer simulation*, Romanian Reports in Physics 68, 294–304 (2016).